

Flash upcycling of spent LiCoO_2 into oxygen-suppressed lithium-replenishing agent for high-performance batteries

Received: 8 August 2025

Accepted: 2 December 2025

Published online: 05 January 2026

Check for updates

Ganxiong Liu^{1,2,6}, Quan Nie^{1,6}, Wang Wan¹, Fangzhou Yang¹, Zhiqi Yang¹, Ge Qu¹, Lingling Guo³, Jitao Chen⁴ ✉, Xuezhe Wei² ✉, Yunhui Huang⁵ ✉ & Chao Wang¹ ✉

Battery recycling is essential to mitigate resource depletion and improve environmental sustainability. However, conventional metallurgical and direct regeneration methods involve trade-offs among energy input, environmental impact, and feedstock adaptability. Here we report a universal upcycling method that converts spent LiCoO_2 into Li_6CoO_4 within 10 seconds via flash Joule heating, achieving complete lithium and cobalt recovery regardless of degradation state. The resulting Li_6CoO_4 serves as a high-capacity sacrificial additive to offset active lithium loss. To overcome its inherent air sensitivity and oxygen release during delithiation, a conformal sulfur coating was applied to stabilize surface chemistry and redirect oxygen evolution into sulfate formation. This sulfur-mediated mechanism effectively suppresses gas generation and parasitic side reactions, enabling non-destructive lithium replenishment. When integrated into graphite || LiFePO_4 pouch cells, the stabilized Li_6CoO_4 achieves 91.4% capacity retention over 1400 cycles at a current density of 80 mA g^{-1} . Comparative life-cycle and techno-economic analyses reveal clear reductions in energy consumption and CO_2 emissions, along with improved economic returns. This work provides a scalable route that bridges positive electrode waste recovery with high-performance lithium supply, advancing closed-loop battery systems for sustainable energy storage.

LiCoO_2 (LCO) is the primary positive electrode material used in rechargeable batteries for portable consumer electronics¹. With the widespread use and frequent replacement of these devices, over 100,000 tons of spent LiCoO_2 (SLCO) batteries are discarded annually worldwide, highlighting the urgent need for sustainable waste management solutions^{2,3}. Current recycling strategies for lithium-ion batteries (LIBs) can be broadly categorized into metallurgy-based elemental extraction and direct regeneration^{4,5}. The former includes

pyrometallurgy, hydrometallurgy, and their combinations, in which the chemical bonds of electrode materials are broken under high-temperature or acidic/alkaline conditions to extract the target metal elements⁶. These methods offer high tolerance for feedstock heterogeneity but compromise economic and environmental sustainability, and are therefore typically regarded as “downcycling” strategies. Additionally, valuable lithium is often lost in the mixed slag or through evaporation at high temperatures, further limiting their overall efficiency⁷.

¹School of Materials Science and Engineering, Tongji University, Shanghai, China. ²School of Automotive Studies, Tongji University, Shanghai, China.

³Shanghai Synchrotron Radiation Facility, Shanghai Institute of Applied Physics, Chinese Academy of Sciences, Shanghai, China. ⁴College of Chemistry and Molecular Engineering, Beijing National Laboratory for Molecular Sciences, Peking University, Beijing, China. ⁵State Key Laboratory of Material Processing and Die & Mould Technology, School of Materials Science and Engineering, Huazhong University of Science and Technology, Wuhan, Hubei, China. ⁶These authors contributed equally: Ganxiong Liu, Quan Nie. ✉ e-mail: chenjitao@pku.edu.cn; weixzh@tongji.edu.cn; huangyh@hust.edu.cn; chaow@tongji.edu.cn

To address these drawbacks, direct regeneration has emerged as a more sustainable alternative, aiming to restore the functional properties of spent electrodes with minimal structural disruption^{8,9}. Typical direct regeneration methods employ molten salt methods, hydrothermal treatments, or solid-state sintering to reconstruct the crystal lattice and revive electrochemical activity¹⁰. This method is particularly well-suited for materials with stable crystal structures, such as olive LiFePO₄ (LFP), where degradation is primarily due to lithium loss^{11,12}. However, for layered oxide materials like LCO and LiNi_xCo_yM₂O₂ (NCM), degradation is induced by intertwined chemical, mechanical, and electrochemical interactions, making direct repair considerably more challenging¹³. While several studies have explored the direct repair of spent LCO into regenerated LCO^{14,15}, achieving stable long-term cycling remains complex. The incomplete performance recovery ultimately results in the inefficient reuse of lithium and cobalt in new cells.

Achieving high resource utilization efficiency requires not only optimized recycling strategies, but also careful consideration of how recovered elements perform during their second life, particularly in long-term cycling stability. In this regard, extending the operational lifespan of LIBs is critical, as it enables fixed lithium inventories to deliver more energy throughout their service life, thereby enhancing overall resource efficiency. Prolonged use not only defers battery retirement but also reduces waste generation and eases the burden of end-of-life battery management. One promising approach to support long-term performance is to supplement cells with an additional lithium supply, which compensates for irreversible lithium loss during cycling and helps minimize capacity fade^{16–18}.

Toward this end, we propose an upcycling strategy that repurposes SLCO into Li₆CoO₄ (L6CO), a high-value sacrificial lithium-replenishing agent. This approach circumvents the need for complex repair of the layered framework required for stable cycling, but instead reconstructs an antifluorite structure that irreversibly releases active lithium to enhance energy density and extend battery lifespan. L6CO does not function as a cycling positive electrode but becomes electrochemically inactive after initial decomposition¹⁹, thus avoiding concerns over long-term stability. The as-prepared L6CO exhibits a low decomposition potential (~ 3.2 V vs. Li⁺/Li), a high irreversible capacity (856 mAh g⁻¹), and great rate capability, outperforming commercially available alternatives such as Li₂NiO₂ (LNO) and Li₅FeO₄ (LFO) in both capacity and oxidation kinetics^{20,21}. The entire conversion is achieved within 10 s via flash Joule heating (FJH). With the simple addition of a lithium source (Li₂O), the residual carbon and polyvinylidene difluoride (PVDF) in the spent electrode are directly utilized as in situ reducing agents during thermal conversion, eliminating the need for external reductants and simplifying the overall process. This method also demonstrates high universality, enabling efficient conversion of SLCO across various degradation states while achieving near-complete recovery of both lithium and cobalt.

Similar to other lithium-rich oxides (e.g., Li₂O, Li₂O₂, and Li₅FeO₄), L6CO suffers from poor air stability due to its high lithium content^{22,23}. In humid environments, it readily reacts with moisture and CO₂ to form LiOH and Li₂CO₃, leading to slurry gelation and complicating storage and processing. While high-temperature carbon coating is commonly used to enhance air stability, forming a dense carbon layer on L6CO is challenging due to the oxidation of carbon and the reduction of transition metals at elevated temperatures. Moreover, oxygen participates in charge compensation during the delithiation of L6CO. The consequent release of lattice oxygen generates reactive oxygen species and O₂ gas^{24,25}, which can trigger parasitic side reactions with the electrolyte and compromise both safety and cycling stability of batteries^{26,27}.

To mitigate these challenges, we introduce a low-temperature sulfur coating strategy to engineer stable L6CO. By leveraging the low melting point and hydrophobicity of elemental sulfur, a uniform and

robust coating can be readily formed on L6CO (L6CO@S), without altering the underlying structural integrity. Beyond physical encapsulation, sulfur exhibits high oxygen-trapping efficiency by chemically interacting with lattice oxygen during charging to form stable SO₄²⁻ species^{28,29}, in which a single sulfur atom coordinates with up to four oxygen atoms. This sulfur-mediated anchoring mechanism effectively suppresses O₂ evolution and mitigates parasitic side reactions. In contrast to conventional carbon coatings that merely act as physical barriers, sulfur provides a chemically active and more effective pathway to stabilize L6CO during initial delithiation.

The as-synthesized L6CO@S composite functions as an effective lithium compensator, offering improved air stability, enhanced processability, and suppressed oxygen evolution. After Li supply with L6CO@S, graphite||LiFePO₄ (Gr||LFP) full cell demonstrates enhanced cycling stability, achieving 91.4% capacity retention after 1400 cycles at 0.5 C (1C = 160 mA g⁻¹), compared to 72% retention in control cells without L6CO@S. It also enhances the capacity retention of graphite||LiCoO₂ (Gr||LCO) cells by 20% over 300 cycles, demonstrating broad applicability across different battery systems. Moreover, utilizing SLCO as a low-cost precursor helps mitigate cobalt-related cost concerns and supports the economic viability of this strategy. Life cycle analysis confirms the reduction in energy consumption and CO₂ emissions, along with improved economic profitability, underscoring the practicality of the upcycling strategy. Together, these findings establish a sustainable route for the high-value reuse of spent batteries in next-generation LIBs.

Results

Rapid upcycling of SLCO into L6CO

The SLCO electrodes were retrieved from degraded 2–10 Ah LCO pouch cells (Supplementary Fig. 1). The electrode materials were efficiently separated from the aluminum current collectors using the water electrolysis-induced separation (WES) method we previously reported³⁰. The collected SLCO pieces were then ground into a fine powder before further processing. The inductively coupled plasma-optical emission spectrometry (ICP–OES) analysis further confirmed that the residual Al content in the SLCO powder was only 1.8 mg L⁻¹, and no Cu impurity was detected (Supplementary Fig. 2). Figure 1a and Supplementary Fig. 3 present the scanning electron microscopy (SEM) morphology of the SLCO material, revealing severe interlayer slippage and microcrack formation on the particle surfaces. These structural degradations are primarily caused by prolonged lithium depletion and mechanical fatigue during repeated Li-ion intercalation/deintercalation cycles. High-resolution transmission electron microscopy (HRTEM) analysis (Fig. 1b) shows that while the bulk SLCO maintains its layered structure, the surface regions undergo partial phase transformation into a disordered spinel structure, with lattice fringes corresponding well to Co₃O₄. X-ray diffraction (XRD) analysis of SLCO (Fig. 1c) further confirms this structural evolution, revealing distinct diffraction peaks corresponding to both the layered LCO phase (PDF# 75-0532) and the spinel Co₃O₄ phase (PDF# 43-1003). Quantitative phase analysis via Rietveld refinement (Supplementary Table 1) indicates that the spinel component accounts for approximately 10 wt%. The formation of densely distributed Co₃O₄ domains at the particle surface markedly impedes lithium-ion diffusion and increase the thermodynamic barriers for the direct restoration of SLCO into new LCO.

Elemental analysis by ICP–OES quantifies a 12% lithium deficiency in SLCO (Li/Co=0.882) relative to stoichiometric LiCoO₂. The degraded material exhibits severely compromised electrochemical performance in half-cells, with an initial capacity of only 67.3 mAh g⁻¹ and rapid capacity fading during cycling (Supplementary Fig. 4). These observations indicate that capacity loss is not solely attributable to lithium depletion but also reflects extensive structural degradation. While high-temperature sintering with stoichiometric lithium compensation

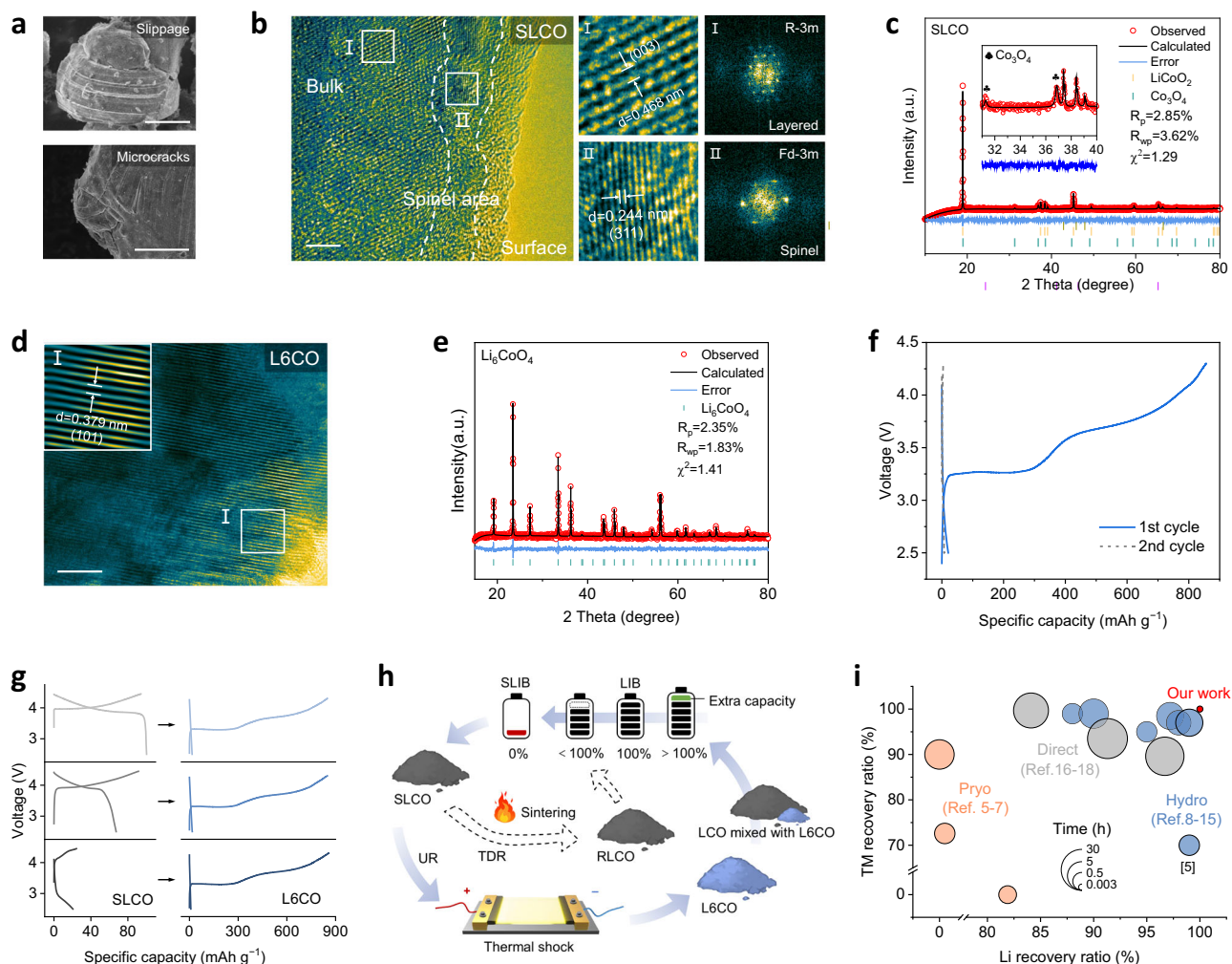


Fig. 1 | Rapid upcycling of SLCO into L6CO. **a** SEM image of SLCO (scale bar, 5 μm). **b** HRTEM of SLCO (scale bar, 5 nm). Region (i) represents the bulk interior of the particle, which retains a layered structure. Region (ii) corresponds to the near-surface area, where a spinel phase is observed. **c** XRD Rietveld refinement results for SLCO. **d** HRTEM images of the upcycled L6CO (scale bar, 5 nm). **e** XRD Rietveld refinement results for the obtained L6CO. **f** Initial charge and discharge curves of L6CO at 0.1C ($1\text{C} = 800\text{ mA g}^{-1}$). **g** Charge and discharge curves of SLCO with varying degrees of degradation (55.7%, 37.1%, 11.4% capacity retention), alongside the corresponding regenerated L6CO. All cells were cycled at 0.1C, with

$1\text{C} = 180\text{ mA g}^{-1}$ for SLCO and $1\text{C} = 800\text{ mA g}^{-1}$ for L6CO. **h** Schematic comparison between traditional direct regeneration (TDR) and the proposed upcycling strategy. Unlike TDR, which aims to restore original structure, the upcycling approach transforms SLCO into L6CO for additional Li supply. Blending L6CO with fresh positive electrodes in new cells markedly improves energy density and cycling stability. **i** Comparison of lithium and TM recovery efficiencies and processing times across different recycling routes. Circle sizes reflect relative time consumption on a logarithmic scale. The numbers in the plot correspond to the article number in Supplementary Table S3.

partially restores crystallinity and capacity, the regenerated material remains inferior to commercial LCO (CLCO), particularly in terms of cycling stability (Supplementary Figs. 5 and 6). These findings underscore the limitations of conventional direct regeneration approaches when applied to severely degraded SLCO, where irreversible phase transformations and structural collapse prevail as dominant degradation mechanisms.

The direct conversion of SLCO to L6CO eliminates the need for complex reconstruction of a precise layered structure. In this approach, SLCO was uniformly mixed with stoichiometric Li_2O and subjected to vacuum sintering via a one-step FJH process. Systematic optimization across a temperature range of 800–1300 $^{\circ}\text{C}$ revealed a clear trend in phase evolution. XRD analysis (Supplementary Fig. 7) shows the gradual disappearance of SLCO-related peaks and the concurrent intensification of L6CO peaks with increasing temperature, indicating improved reaction completeness. At 1200 $^{\circ}\text{C}$, a 10 s pulse enables complete conversion into phase-pure Li_6CoO_4 , whereas further increases in temperature or dwell time do not improve the transformation and instead incur unnecessary energy input

(Supplementary Fig. 8). Thus, 1200 $^{\circ}\text{C}$ for 10 s was identified as the optimal synthesis condition, balancing transformation kinetics with energy efficiency. The corresponding temperature–time profile during the FJH process (Supplementary Fig. 9) shows that the sample temperature rises sharply to 1200 $^{\circ}\text{C}$, confirming the fast heating characteristics of this technique.

The resulting product exhibits a distinct blue coloration (Supplementary Fig. 10). HRTEM analysis identifies well-ordered lattice fringes with an interplanar spacing of 0.379 nm, corresponding to the (101) planes in the antifluorite structure (Fig. 1d and Supplementary Fig. 11). XRD analysis and Rietveld refinement (Fig. 1e and Supplementary Table 2) reveal a phase-pure L6CO diffraction pattern, with complete elimination of LCO and Co_3O_4 signals and no detectable impurities, demonstrating the effectiveness of the FJH approach for rapid and complete phase conversion.

Our FJH upcycling strategy offers a distinct advantage over conventional direct recycling methods by eliminating the need for complete removal of PVDF binders and conductive carbon prior to regeneration³¹. Instead, these residual components are strategically

utilized, serving as in situ reducing agents that facilitate efficient cobalt reduction during the formation of L6CO. This eliminates the need for both extensive pre-treatment steps and external reductants. Microstructural characterization (Supplementary Fig. 12) confirms that the high temperatures during FJH effectively decompose residual carbon and PVDF in pristine SLCO. The resulting L6CO exhibits a smooth single-crystal morphology, indicating the complete removal of surface contaminants. FTIR of SLCO displays characteristic absorption peaks corresponding to PVDF (900–1400 cm^{-1}), which almost completely disappear after FJH (Supplementary Fig. 13), confirming its full decomposition. Owing to the brief reaction duration, the released fluorinated volatiles are transient and concentrated in the off-gas stream, which makes them amenable to engineering control. This self-contained upcycling protocol clearly simplifies battery recycling workflows while maintaining stringent purity standards. EDS elemental mapping shows a homogeneous distribution of cobalt and oxygen throughout the particles, confirming compositional uniformity (Supplementary Fig. 14).

Electrochemical evaluation demonstrates promising lithium compensation capability of L6CO (Fig. 1f), with an initial charge capacity of 856.2 mAh g^{-1} at 0.1 C (1 C = 800 mA g^{-1}). The voltage profile exhibits two well-defined oxidation plateaus at 3.25 V and 3.65 V (vs. Li^+/Li), with negligible discharge capacity (<2.5% of charge capacity), characteristic of an efficient lithium reservoir. Cyclic voltammetry (CV) profiles further corroborate these electrochemical characteristics, showing great alignment between oxidation peaks and galvanostatic plateaus (Supplementary Fig. 15). Notably, L6CO maintains high rate performance (Supplementary Fig. 16), delivering 759 mAh g^{-1} at 0.5 C (88.6% retention compared to 0.1 C), outperforming commercial LFO references, which retain only 57.6% of their capacity under identical testing conditions (Supplementary Fig. 17). The enhanced oxidation kinetics enable complete decomposition during the first cycle and suppress parasitic reactions during subsequent cycling.

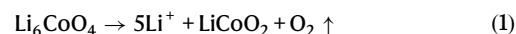
Unlike conventional regeneration methods that struggle with the variable degradation of different SLCO materials, our approach demonstrates great versatility. We systematically evaluated three SLCO samples with varying degradation levels from different spent batteries, with initial capacities ranging from 20.5 to 100.3 mAh g^{-1} and corresponding Li/Co ratios between 0.774 and 0.882. Remarkably, regardless of the initial degradation state, all samples were successfully transformed into phase-pure L6CO with precise stoichiometric control, as confirmed by ICP-OES analysis (Supplementary Fig. 18). Additionally, the upcycled products exhibited consistent electrochemical performance, each delivering charge capacity of approximately 850 mAh g^{-1} (Fig. 1g). To simulate a broader range of degradation conditions, fresh LCO was blended with varying amounts of Co_3O_4 (5–50 wt.%) and a controlled amount of carbon black was added as the reducer. Despite these deliberate compositional variations, FJH consistently yielded phase-pure L6CO (Supplementary Fig. 19). This consistency underscores the robustness of our method for practical application across diverse SLCO feedstocks.

Figure 1h schematically illustrates our closed-loop upcycling strategy, where the regenerated L6CO acts as a high-efficiency Li supply additive. When combined with fresh positive electrode materials, it enables lithium inventory exceeding 100% in next-generation battery systems. This approach simultaneously extends battery service life and maximizes energy output from limited lithium resources, demonstrating high resource efficiency for both upcycling and reuse. In contrast to conventional regeneration methods, which require precise phase control and customized calcination protocols for different feedstocks but still fail to achieve complete electrochemical recovery and high resource recovery efficiency, our method offers clear improvements. Quantitative comparisons (Fig. 1i and Supplementary Table 3) demonstrate that our approach outperforms

conventional recycling in both material recovery and temporal efficiency. The rapid thermal kinetics of FJH effectively suppress lithium volatilization and enabling near-100% recovery of both lithium and cobalt (Supplementary Fig. 20), while reducing processing times by over an order of magnitude. Together, these advantages establish a grave-to-cradle pathway that unites sustainable upcycling with practical reusability.

Engineer stable L6CO through sulfur coating

The high lithium content of L6CO renders it inherently unstable in ambient air. Its highly alkaline surface readily reacts with moisture, leading to gelation of electrode slurries during electrode fabrication. Upon oxidation, each mole of L6CO decomposes to release five moles of Li^+ and one mole of O_2 , forming a solid disordered- LiCoO_2 residue, as demonstrated by Eq. (1):



The substantial O_2 evolution poses safety challenges and induces undesirable side reactions. To address these drawbacks and enhance practical processability, a sulfur coating strategy was employed. Elemental sulfur was uniformly coated onto L6CO via a low-temperature thermal treatment at 160 °C. The resulting L6CO@S exhibits a noticeable color change from blue to green (Supplementary Fig. 21), confirming the formation of a conformal sulfur layer.

SEM images of L6CO@S reveal a smooth and uniform particle surface following sulfur coating, with no observable aggregation of sulfur particles (Supplementary Fig. 22). Transmission electron microscopy (TEM) image coupled with EDS elemental mapping reveals a homogeneous sulfur distribution across the surface (Fig. 2a). Cryo-TEM further confirms a continuous and conformal sulfur coating that fully encapsulates the L6CO particles, with an average thickness of approximately 20 nm (Fig. 2b and Supplementary Fig. 23). XRD patterns (Supplementary Fig. 24) show only the characteristic peaks of crystalline L6CO, with no detectable peaks corresponding to crystalline sulfur, indicating that sulfur remains in an amorphous state while the L6CO core structure is well preserved. Importantly, the sulfur coating does not compromise the electrochemical performance of L6CO. Even with a sulfur content as high as 10 wt.%, L6CO@S still delivers a high initial charge capacity of 627.9 mAh g^{-1} at 0.5 C (1 C = 600 mA g^{-1}), confirming that lithium extraction remains efficient despite the surface modification (Supplementary Fig. 25). Moreover, galvanostatic intermittent titration technique (GITT) measurements reveal that the Li^+ diffusion coefficients (D_{Li}) of pristine L6CO and L6CO@S remain in the same order of magnitude before and after coating (Supplementary Fig. 26), indicating that lithium-ion transport is not markedly hindered by the sulfur layer. In situ XRD analysis during charging up to 4.3 V reveals a progressive attenuation of the (101) and (201) diffraction peaks of L6CO (Fig. 2c), reflecting a transition from long-range crystalline order to a more disordered structure upon lithium extraction.

Improved air stability for L6CO@S. The air stability of both pristine L6CO and L6CO@S was systematically evaluated through gravimetric, structural, and electrochemical analyses after exposure to ambient conditions (relative humidity, 30% RH). The uncoated L6CO also shows a noticeable color transformation from blue to bluish-gray after 72 h of exposure (Fig. 2d), visually indicating chemical degradation due to surface reactions with ambient H_2O and CO_2 . Gravimetric analysis that pristine L6CO undergoes rapid degradation, with a 12% mass gain after 72 h due to the formation of surface hydroxides and carbonates. In contrast, L6CO@S exhibits improved stability, showing only -1% mass increase under identical conditions (Fig. 2e). XRD patterns of both L6CO and L6CO@S after exposure to 30% relative humidity at different time points are shown in Fig. 2f and Supplementary Fig. 27. After

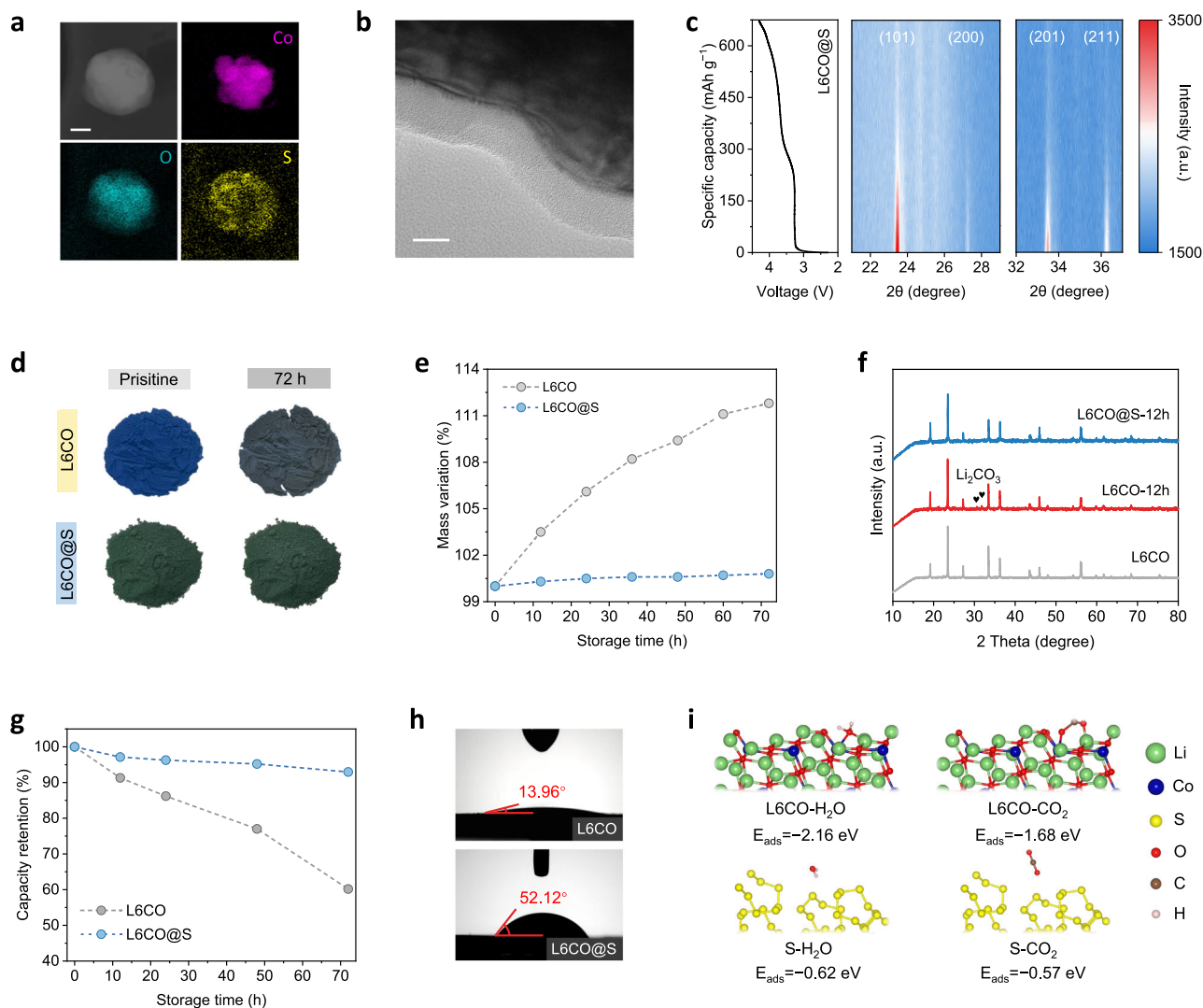


Fig. 2 | Improved Air stability for L6CO@S. **a** TEM image and corresponding EDS elemental mapping of L6CO@S (scale bar, 100 nm). **b** Cryo-TEM images of the sulfur coating layer on L6CO@S (scale bar, 20 nm). **c** In situ XRD spectra of L6CO@S during the first charge process (0.1 C, 1 C = 600 mA g⁻¹). **d** Optical images of L6CO and L6CO@S powders before and after 72 h storage in air (30% relative humidity, RH). **e** Mass evolution of L6CO and L6CO@S upon exposure to ambient air (30% RH) for varying durations. **f** XRD patterns of L6CO and L6CO@S powders

before and after 12 h exposure to air (30% RH). **g** Evolution of specific capacities of L6CO and L6CO@S upon exposure to ambient air (30% RH) for varying durations. **h** Contact angle measurements between water droplets and the surfaces of L6CO and L6CO@S, which were compressed to pellets under 6 MPa pressure prior to testing. **i**, Calculated adsorption energies of H₂O and CO₂ molecules on the surface of L6CO and on the sulfur layer of L6CO@S.

12 h, L6CO develops prominent peaks corresponding to Li₂CO₃, indicating severe surface degradation, while L6CO@S shows no detectable degradation products even after 48 h. SEM images in Supplementary Fig. 28 further confirms this contrast: after 24 h in 30% RH air, L6CO develops flaky alkaline surface residues, whereas L6CO@S maintains a clean, smooth particle surface.

Electrochemical testing further underscores the protective effect of the sulfur coating. After 72 h of exposure to 30% RH air, uncoated L6CO retains only 61.2% of its initial capacity, whereas L6CO@S maintains 92.9%, delivering 634.6 mA h g⁻¹ (Fig. 2g and Supplementary Fig. 29). Even under harsher conditions (60% RH for 48 h), L6CO@S retains 88.8% of its original capacity (Supplementary Fig. 30). Beyond performance decay, surface degradation also introduces great processing challenges. After 24 h in 30% RH air, uncoated L6CO induces strong gelation due to its surface alkalinity, while slurry containing L6CO@S remains well-dispersed and flowable (Supplementary Fig. 31). These results highlight the high environmental tolerance and manufacturing compatibility of L6CO@S.

Contact angle measurements demonstrate a clear improvement in water resistance after sulfur coating. The water contact angle increases dramatically from 13.96° for uncoated L6CO to 52.12° for the L6CO@S composite (Fig. 2h), highlighting the coating's effectiveness in enhancing surface hydrophobicity. This effect is also visually corroborated: water droplets rapidly spread and trigger a blue-to-yellow color change on uncoated L6CO, reflecting immediate surface reactions. In stark contrast, droplets remain nearly spherical on L6CO@S for over 1 minute without inducing any visible color change (Supplementary Fig. 32), demonstrating the coating's effectiveness in suppressing H₂O-driven degradation. We calculated the adsorption energies of H₂O and CO₂ molecules on the (101) surface of L6CO (Fig. 2i). Both molecules interact through their oxygen atoms coordinating with surface metal sites (Li and Co), resulting in strong adsorption energies of -2.16 eV for H₂O and -1.68 eV for CO₂. These values highlight the pronounced reactivity of L6CO toward ambient moisture and carbon dioxide. In contrast, when the sulfur coating is applied, the adsorption occurs instead on the sulfur surface layer,

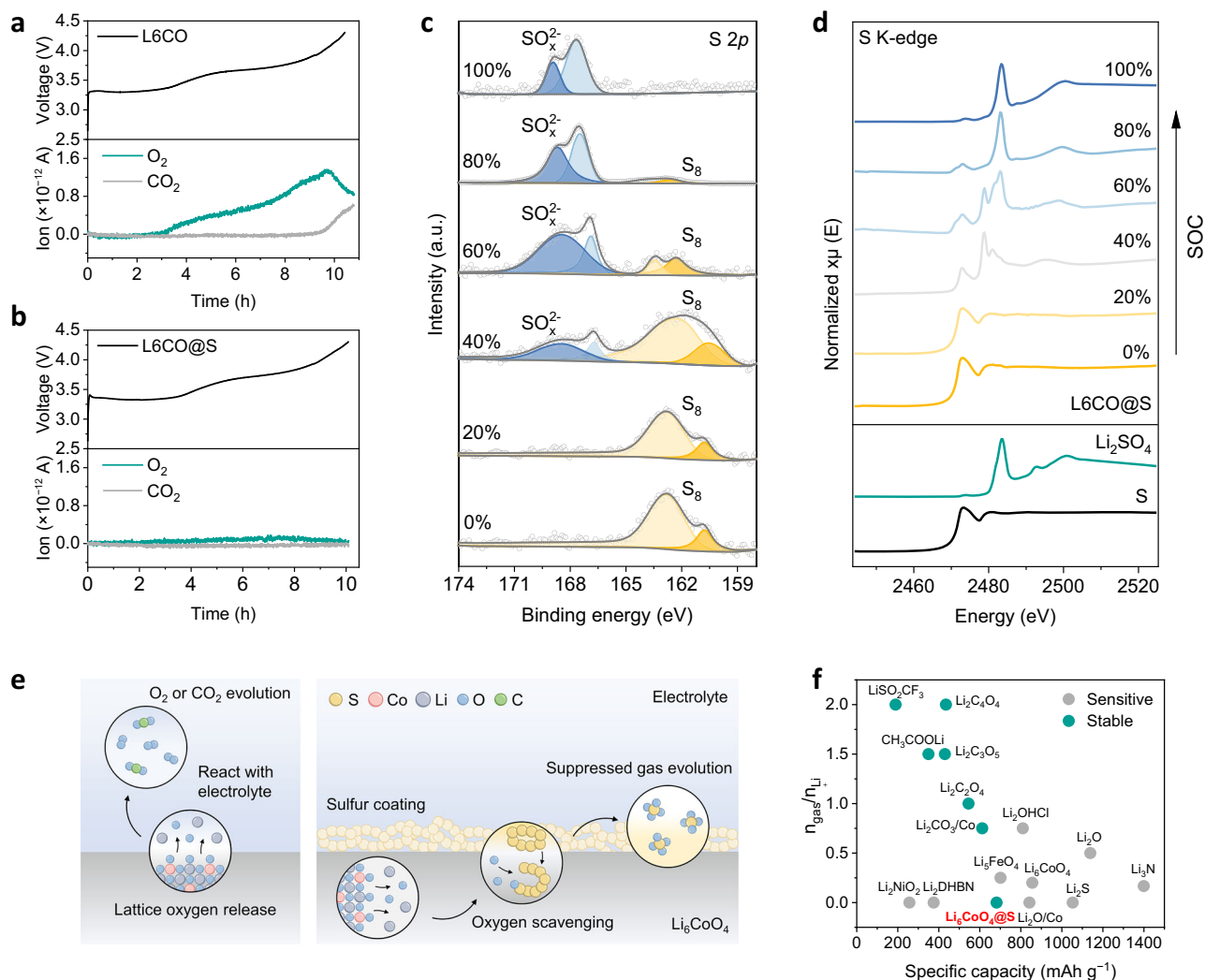


Fig. 3 | Sulfur-driven suppression of oxygen evolution in L6CO@S. a, b OEMS spectra of L6CO and L6CO@S during the first charge process at 0.1 C, measured at 25 °C. **c** S 2p XPS spectra of L6CO@S electrodes collected at various states of charge (SOC, from 0 to 100%) during the first charging process at 0.1 C. **d** S K-edge XANES spectra of L6CO@S electrodes at different SOC during the first charging

process at 0.1 C. **e** Schematic illustration of sulfur-induced suppression of lattice oxygen release in L6CO@S. **f** Comparison of specific capacities and the corresponding gas evolution per mole of Li⁺ released ($n_{\text{gas}}/n_{\text{Li}^+}$) for representative lithium replenishment agents.

where the interactions are considerably weaker. The adsorption energies are reduced to -0.62 eV for H₂O and -0.57 eV for CO₂, indicating a substantial suppression of surface affinity for these molecules. These striking contrasts highlight the sulfur layer as a robust barrier that shields L6CO from atmospheric exposure.

Suppressed oxygen evolution for L6CO@S. The gas evolution behavior of L6CO and L6CO@S was systematically investigated via online electrochemical mass spectrometry (OEMS). For pristine L6CO, charge compensation during the initial ~30% state of charge (SOC) is primarily achieved through the oxidation of Co²⁺, with no detectable O₂ evolution. Beyond this point, lattice oxygen begins to participate in the oxidation process, resulting in apparent O₂ release (Fig. 3a). At higher voltages, a rise in CO₂ signals was observed, attributed to electrolyte decomposition triggered by reactive oxygen species such as oxygen radicals (O•), peroxide anions (O₂²⁻), or singlet oxygen (¹O₂)³². In contrast, L6CO@S exhibited nearly complete suppression of gas evolution, with O₂ and CO₂ signals remaining close to background levels and no detectable SO₂ formation (Fig. 3b and Supplementary Fig. 33). This complete inhibition of gas evolution underscores the dual

protective function of the sulfur layer: stabilizing lattice oxygen and mitigating electrolyte decomposition at high voltages.

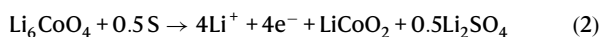
The oxidation state of sulfur was further examined using X-ray photoelectron spectroscopy (XPS) analysis of L6CO@S at different SOC (Fig. 3c). Upon charging, the S 2p spectra shift from the characteristic peaks of elemental sulfur (~ 162.5 eV) to a new peak at ~ 168.5 eV, corresponding to the S–O bond in SO₄²⁻. This transformation indicates the involvement of sulfur in charge compensation. XPS depth profiling yielded consistent results across different etching depths (Supplementary Fig. 34), confirming that the transformation is spatially uniform across the particle surface. Importantly, this sulfur oxidation process is not driven by cobalt but is instead closely associated with the presence of reactive lattice oxygen. A control experiment using sulfur-coated LCO, synthesized via the same method, showed negligible sulfur oxidation when charged to 4.3 V (Supplementary Fig. 35). This result is consistent with LCO's minimal oxygen release at this voltage, further confirming the critical role of lattice oxygen in driving sulfur oxidation. In addition, we evaluated the air stability of the sulfur coating. S 2p XPS spectra of L6CO@S stored in air for 3 and 7 days showed no evidence of sulfate formation

(Supplementary Fig. 36), indicating that the sulfur does not undergo spontaneous oxidation in ambient conditions. The oxidation to sulfate in our system requires both electrochemical driving force and the presence of highly reactive oxygen species.

X-ray absorption spectroscopy (XAS) measurements were conducted to gain further insight. The S K-edge X-ray absorption near-edge structure (XANES) spectra reveal the valence evolution of sulfur (Fig. 3d). The pristine L6CO@S electrode exhibits an absorption edge that coincides with elemental sulfur. From 0% to 40% state of charge (SOC), charge compensation is dominated by Co oxidation, and the S K-edge spectrum remains unchanged, indicating no sulfur oxidation. Between ~40% and 60% SOC, a transient feature appears between the positions of elemental sulfur and Li₂SO₄, consistent with short-lived partially oxidized sulfur species (e.g., sulfites), which disappear at higher SOC. Beyond 60% SOC, the edge shifts toward higher energy, with the emergence of features at 2478.6 eV and 2483.4 eV, characteristic of sulfate species. At full charge, the spectrum nearly overlaps with that of Li₂SO₄, confirming the complete oxidation of sulfur to SO₄²⁻. Capillary electrophoresis was further employed to quantify SO₄²⁻ in fully charged L6CO@S electrodes. The measured concentration (~39 ppm) closely matched the theoretical value (Supplementary Fig. 37), providing independent confirmation of complete sulfur oxidation.

The evolution of the Co oxidation state during charge was also examined via Co K-edge XAS. The XANES spectra (Supplementary Fig. 38) show that both L6CO and L6CO@S undergo oxidation from +2 to +4 as delithiation progresses. Notably, at 50% SOC, L6CO@S exhibits a slightly lower Co oxidation state compared to bare L6CO, suggesting partial charge compensation by sulfur. Upon further charging, a shift of the Co K-edge to lower energy is observed, consistent with lattice oxygen oxidation and partial Co–O bond breaking. At 100% SOC (4.3 V), both L6CO and L6CO@S show a Co near-edge shift to lower energy relative to LCO, which can be attributed to further Co–O bond breaking and ligand-to-metal charge transfer, leading to the formation of Co₃O₄-like phases with a lower average Co oxidation state. FT-EXAFS spectra (Supplementary Fig. 39) reveal a concurrent increase in Co–O coordination, indicating a transformation of the Co environment from tetrahedral to octahedral as lithium is extracted. Wavelet transform analysis (Supplementary Fig. 38) confirms that Co is only coordinated to O or Co neighbors, with no Co–S or Co–S–O coordination detected. ICP–OES analysis of the electrolyte and XPS characterization of the graphite electrode after oxidation confirm the absence of cobalt dissolution or deposition in the electrolyte or on the negative electrode, ruling out the formation of CoSO₄, which would easily dissolve in the electrolyte (Supplementary Figs. 40 and 41).

Based on the experimental findings, we propose the following sulfur-mediated oxygen fixation mechanism:



Gibbs free energy calculations further support this mechanism (Supplementary Fig. 42). The oxidation pathway of L6CO@S leading to Li₂SO₄ exhibits a lower Gibbs free energy ($\Delta G = 593.71 \text{ kJ mol}^{-1}$) compared to direct oxygen evolution from L6CO ($\Delta G = 1374.52 \text{ kJ mol}^{-1}$). Additionally, the formation of CoSO₄ has a higher Gibbs free energy ($\Delta G = 1052.0 \text{ kJ mol}^{-1}$) than that of Li₂SO₄, indicating that Li₂SO₄ formation is thermodynamically favored. This conclusion aligns with our experimental observations, confirming that sulfur preferentially forms Li₂SO₄ rather than CoSO₄.

The proposed reaction mechanism is illustrated schematically in Fig. 3e. Upon charging, S₈ molecules may be attacked by reactive oxygen species, leading to S–S bond cleavage and the formation of generating reactive chain-like sulfur intermediates (e.g., [S₈]^{•+}, [S₅]^{•+}, etc.)³³. These intermediates gradually react with oxygen species to form SO₄²⁻, leading to the irreversible formation of thermodynamically

stable Li₂SO₄. While this mechanism entails a slight compromise in capacity, the oxidation of sulfur to sulfate, rather than the release of gaseous byproducts, markedly suppresses gas-induced side reactions and associate safety concerns. This strategy offers a viable approach to oxygen regulation in high-capacity battery systems through surface oxidation mediators. A comparative analysis between L6CO@S and a range of representative lithium replenishment agents is shown in Fig. 3f and summarized in Supplementary Table 4. Key characteristics, including capacity, decomposition voltage, air stability, and gas evolution, were systematically evaluated. Our proposed L6CO@S demonstrates a well-balanced performance across all four dimensions, highlighting its strong potential for practical application.

Non-destructive Li supply for extended cycle life

The lithium compensation performance of both pristine and sulfur-coated L6CO was quantitatively assessed in Gr||LFP full cells containing 4 wt.% additive. As shown in Fig. 4a, all cells were charged at a constant current of 0.1 C (1 C = 160 mA g⁻¹) in the initial cycle, with a cutoff voltage of 4.3 V to ensure complete decomposition of the lithium supply additive. To determine the real decomposition ratio of L6CO@S when coupled with LiFePO₄, additional tests were conducted at 0.1–1 C in Li||LFP+L6CO@S half-cells (Supplementary Fig. 43), showing that the additive is nearly fully oxidized even at 1 C, confirming its compatibility with high-rate formation step. The incorporation of either L6CO or L6CO@S resulted in a pronounced extension of the charge plateau, reflecting the additional lithium input from the additive, and led to a marked increase in cell capacity. The Gr||LFP+4% L6CO@S cell delivered high initial capacities of 205.2 mAh g⁻¹ (charge) and 159.3 mAh g⁻¹ (discharge), approaching the theoretical limit defined by Li||LFP half-cell measurements (Supplementary Fig. 44). This result indicates near-complete restoration of lithium inventory in the full-cell configuration. The rate performance of the LFP full cells also showed improvement with the addition of L6CO and L6CO@S (Supplementary Fig. 45). The long-term cycle stability was further evaluated. After 800 cycles at 0.5 C (1 C = 160 mA g⁻¹), the L6CO@S-based cell retained 92.3% of its initial capacity, markedly outperforming the L6CO counterpart, which exhibited accelerated capacity fade after 500 cycles and retained only 86.8% after 800 cycles (Fig. 4b). Throughout the extended cycling, cells with L6CO@S achieved a high average Coulombic efficiency of 99.993% (Fig. 4c), underscoring the coating's role in suppressing parasitic side reactions and ensuring stable long-term performance.

In situ electrochemical impedance spectroscopy (EIS) was used to monitor impedance evolution during the initial charging process (Fig. 4d). The Gr||LFP+4% L6CO cell exhibited a progressive increase in impedance as the state of charge (SOC) rose, while the Gr||LFP+4% L6CO@S cell maintained more stable impedance characteristics. Complementary EIS measurements after the 1st, 10th, and 30th cycles revealed a notable increase in resistance for the Gr||LFP+4% L6CO cell (Supplementary Fig. 46), while the Gr||LFP+4% L6CO@S cell showed minimal impedance growth over time. Post-cycling SEM analysis revealed the structural origins of this disparity. The uncoated L6CO electrodes exhibited numerous gas-induced voids and pronounced delamination between the active material layer and the current collector (Fig. 4e and Supplementary Fig. 47), while the L6CO@S electrodes maintained great structural integrity and interfacial adhesion. This morphological contrast can be attributed to gas evolution, as reported in our previous study, where gas generation was found to degrade the electrode structure and lead to the deterioration of electrochemical performance. Moreover, reactive oxygen intermediates chemically attack both electrolyte components and the SEI layer, accelerating impedance growth.

In situ ultrasonic transmission imaging was used to monitor gas evolution during the initial charge process in pouch cells. Leveraging

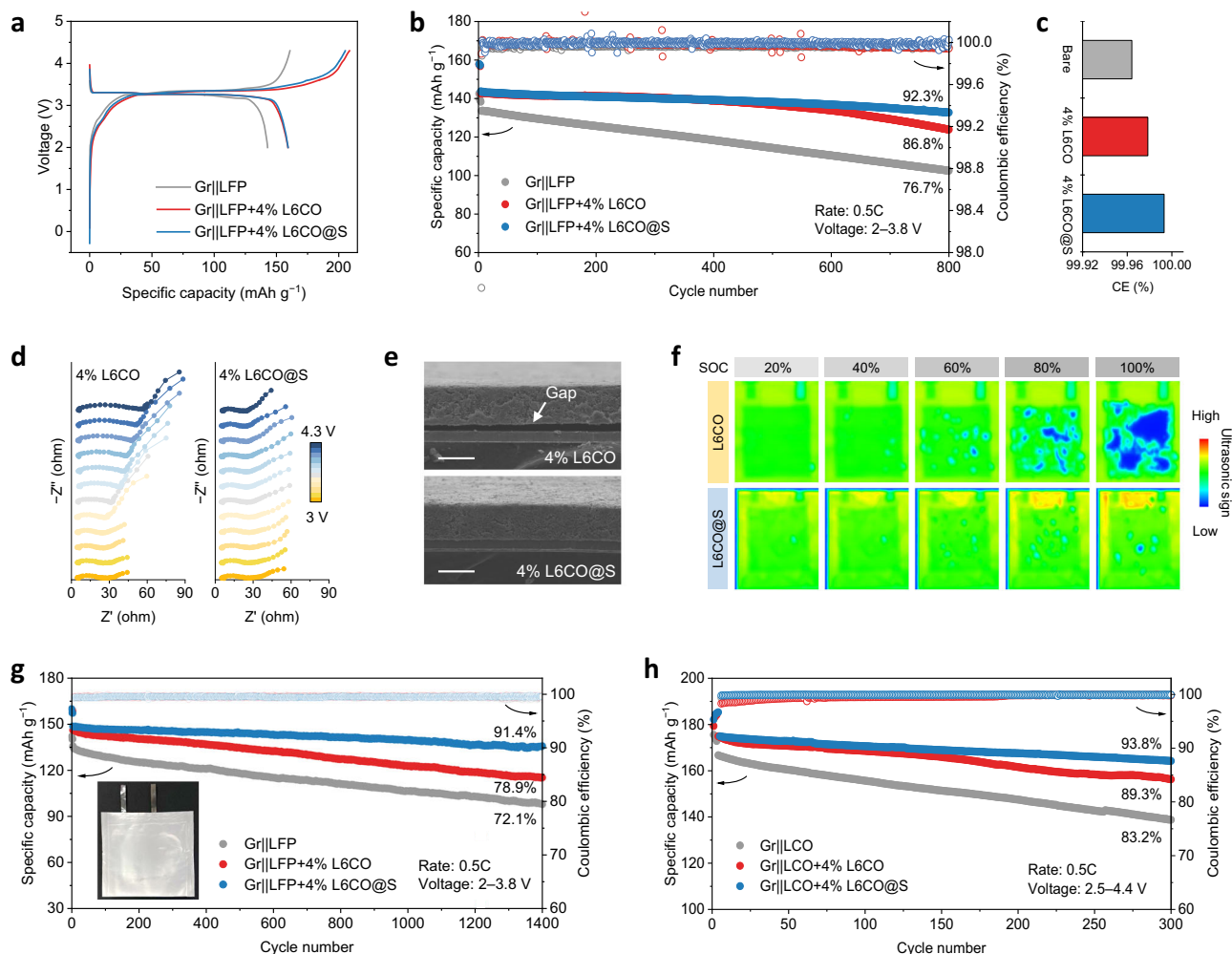


Fig. 4 | Electrochemical performance of L6CO@S as a nondestructive Li supply.

a Initial charge/discharge curves of Gr||LFP full cells with and without additional lithium supply at 0.1C ($1\text{C} = 160\text{ mA g}^{-1}$). **b** Long-term cycling performance (**b**) and average coulombic efficiencies during 800 cycles (**c**) of Gr||LFP, Gr||LFP + 4% L6CO, and Gr||LFP + 4% L6CO@S full cells at 0.5C ($1\text{C} = 160\text{ mA g}^{-1}$). **d** In situ EIS spectra of Gr||LFP + 4% L6CO and Gr||LFP + 4% L6CO@S cells during the first charging process at 0.1C. **e** Cross-sectional SEM images of LFP electrode with 4%

L6CO and 4% L6CO@S after the first cycle (scale bar, 50 μm) at 0.1C. **f** In situ ultrasonic transmission mappings of Gr||LFP + 4% L6CO and Gr||LFP + 4% L6CO@S pouch cells during initial charging at 0.1C ($1\text{C} = 160\text{ mA g}^{-1}$), visualizing gas evolution. **g** Cycling performance of Gr||LFP, Gr||LFP + 4% L6CO, and Gr||LFP + 4% L6CO@S pouch full cells at 0.5C. **h** Cycling performance of Gr||LCO, Gr||LCO + 4% L6CO, and Gr||LCO + 4% L6CO@S full cells at 0.5C ($1\text{C} = 180\text{ mA g}^{-1}$). All cells were tested at 25 °C.

the high acoustic impedance at the gas–liquid interfaces, ultrasound is highly sensitive to the emergence of gas species. As shown in Fig. 4f, the Gr||LFP + 4% L6CO cell exhibited gas generation starting at ~60% SOC, with progressive accumulation toward full charge (100% SOC), eventually forming large gas pockets. It is worth noting that, due to the contribution of LFP to overall capacity in the full cell, the onset of gas evolution appears at a higher SOC compared to the ~30% SOC observed in the pure L6CO OEMS test. In contrast, L6CO@S-modified cells maintained consistently high ultrasound transmittance throughout the charging process, showing negligible gas production. These results provide direct visual evidence of the sulfur coating's effectiveness in suppressing oxygen evolution from L6CO decomposition and subsequent electrolyte oxidation.

To further validate the practical applicability of L6CO@S, its long-term performance was evaluated in Gr||LFP pouch full cells. As shown in Fig. 4g, Gr||LFP pouch cell incorporating L6CO@S delivers an initial discharge capacity that is 12.6% higher than that of control cell, and the improvement becomes more pronounced with extended cycling. After 1400 cycles at 0.5C ($1\text{C} = 160\text{ mA g}^{-1}$), the capacity enhancement reaches 38.7%, with an overall capacity retention of 91.4%. The

corresponding charge/discharge profiles (Supplementary Fig. 48) show minimal polarization growth throughout cycling, indicating well-preserved electrode structure and reaction kinetics. Ultrasonic imaging after 1400 cycles reveals no detectable gas accumulation (Supplementary Fig. 49), and visual inspection shows no swelling of the pouch cell (Supplementary Fig. 50). These collective findings further highlight the critical role of sulfur coating in mitigating gas evolution and enhancing the long-term electrochemical stability. To demonstrate industrial scalability, we further fabricated ampere-hour-scale Gr||LFP pouch cells incorporating L6CO@S additives. As shown in Supplementary Fig. 51, the full-scale cell exhibits great lithium compensation efficacy while maintaining stable cycling performance, confirming seamless integration with commercial manufacturing processes and cell designs. The 1 Ah pouch cell also showed no visible swelling even after 450 cycles (Supplementary Fig. 52). This successful scale-up represents a critical step toward industrial implementation of our upcycling strategy.

The advantages of L6CO@S extend beyond LFP systems to LCO-based full cells. In the Gr||LCO configuration, both initial capacity and cycle life were substantially improved (Supplementary Fig. 53), with

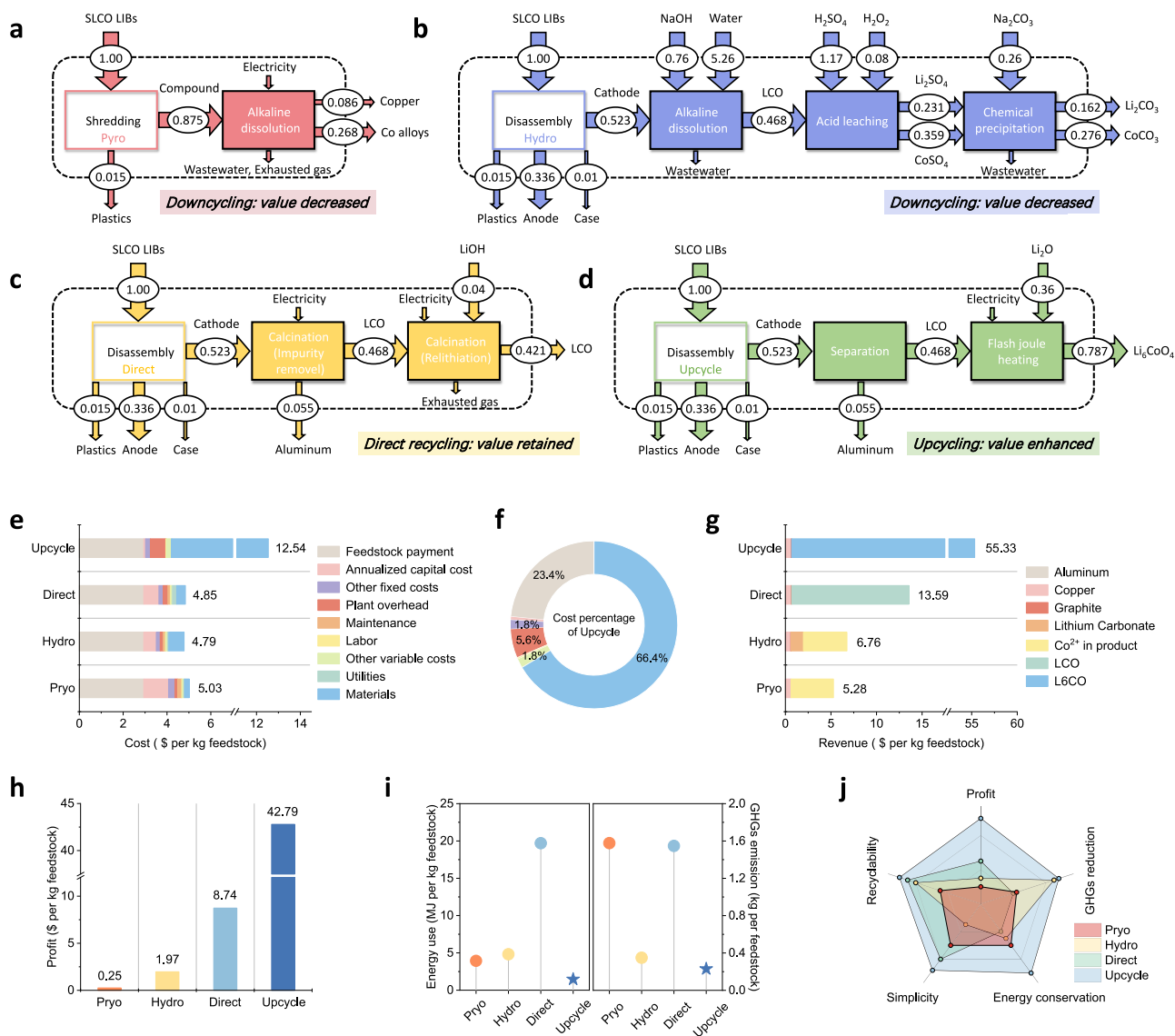


Fig. 5 | Economic and environmental analysis of different SLCO recycling strategies. Material flow analysis of various SLCO recycling routes, showing the life cycle inventory with all relevant inputs and outputs: **a** Pyrometallurgical method, **b** hydrometallurgical method, **c** Traditional direct recovery method, and **d** our proposed upcycling method. **e–j** Techno-economic analysis of the Pyro, Hydro, Direct, and Upcycle processes: **e** Cost analysis. **f** Cost proportions of the upcycle process. **g** Revenue analysis. **h** Profit calculations. **i** Greenhouse gas (GHG) emission and total energy consumption. **j** Comprehensive comparison of different recycling technologies.

Direct, and Upcycle processes: **e** Cost analysis. **f** Cost proportions of the upcycle process. **g** Revenue analysis. **h** Profit calculations. **i** Greenhouse gas (GHG) emission and total energy consumption. **j** Comprehensive comparison of different recycling technologies.

capacity retention rising from 83.2% to 93.8% after 300 cycles (Fig. 4h). These results underscore the broad applicability of L6CO@S across different battery systems and highlight its strong potential as a universal lithium-replenishing additive for advanced lithium-ion batteries.

Economic and environmental analysis

A closed-loop life cycle analysis (LCA) was conducted using the EverBatt 2023 model developed by Argonne National Laboratory to systematically compare the economic and environmental impacts of various recycling approaches. Detailed calculation information is available in the Supplementary Data. Figure 5a–d provides a comprehensive comparison of mainstream battery recycling technologies, along with detailed material flow analyses. Using one ton of spent LCO batteries as an example, approximately 523 kg of SLCO material and 336 kg of negative electrode material can be recovered. Pyrometallurgical recycling involves high-temperature co-smelting of both electrodes, producing metallic alloys such as Co/Cu, while lithium is mostly lost to the slag, resulting in lower overall recovery efficiency

and limited product value. In contrast, hydrometallurgical processes use acid-base leaching followed by precipitation to extract lithium and cobalt, ultimately producing about 162 kg of Li_2CO_3 and 276 kg of CoCO_3 . Direct regeneration allows the recovery of high-value LCO material. After accounting for process losses and non-repairable LCO, the average yield reaches approximately 421 kg, which is equivalent to 90% of the input SLCO mass. In comparison, our upcycling strategy enables the production of L6CO with higher added value. This process features a streamlined workflow with minimal material loss, avoids extensive acid and base usage, and drastically reduces energy consumption. As a result, approximately 787 kg of L6CO can be obtained.

The energy consumption, greenhouse gas (GHG) emissions, cost-revenue balance, and profitability of various recycling processes were quantitatively assessed. As shown in Fig. 5e, the total recycling costs per kilogram of feedstock are \$5.03 (Pyro), \$4.79 (Hydro), \$4.85 (Direct), and \$12.54 (Upcycle). Despite the higher cost of the Upcycle method, 89.8% of this cost is attributed to raw materials (Fig. 5f), rather than energy or infrastructure, indicating high value addition rather

than process inefficiency. Revenue analysis (Fig. 5g) shows that the Pyro and Hydro routes yield low-value alloys or salts, while Direct recycling produces regenerated LCO with better marketability. The Upcycle process outperforms all other routes by producing L6CO, a high-performance lithium-replenishment material with great economic potential. Notably, L6CO can be synthesized at an estimated cost of ~\$16,000 per ton. Since L6CO is not yet commercially available, we benchmarked its price against LFO (~\$69,500 per ton), one of the most representative lithium-rich sacrificial additives already produced at scale. Both L6CO and LFO share an anti-fluorite structure and exhibit suitable decomposition voltages with high irreversible capacities, with L6CO delivering slightly improved electrochemical performance. This pronounced cost–performance advantage highlights the commercial viability and differentiated value of L6CO within next-generation battery manufacturing.

Figure 5h illustrates that the upcycle route delivers the highest profit margin of \$42.79 per kilogram of raw material, demonstrating strong economic feasibility. The GHG emissions, shown in Fig. 5i, reveal that the upcycling strategy has the lowest emissions among all methods, at 0.23 kg per kg of feedstock. The rapid Joule heating process also ensures high energy efficiency, consuming just 1.461 MJ per kg of feedstock, considerably less than conventional thermal or wet chemical approaches.

A comprehensive comparison of recycling strategies (Fig. 5j) underscores the superiority of our upcycling approach across multiple dimensions, including profitability, simplicity, recyclability, energy consumption, and GHG emissions. Based on the estimated disposal volume of SLCO batteries in 2024, converting all this waste could yield ~78,700 metric tons of L6CO. This would be sufficient to meet the Li supply demand of ~2.6 million metric tons of LFP materials (assuming a 3 wt.% L6CO additive), exceeding the projected global LFP output of ~2.4 million metric tons in 2024. These figures underscore the potential of this upcycling strategy to alleviate lithium shortages amid the rapid expansion of energy storage and electric vehicle markets. The broader implications of L6CO upcycling method provides a scalable solution that directly transforms waste into performance-enhancing additives, simultaneously improving both sustainability and electrochemical performance throughout the lithium-ion battery value chain.

Discussion

This work presents a rapid and scalable upcycling strategy that converts SLCO into high-performance, high-value L6CO using FJH. Unlike conventional regeneration methods that rely on complex phase reconstruction for stable cycling, L6CO serves as an additional Li supply that undergoes an irreversible oxidation step without participating in subsequent cycles. The process achieves complete phase transformation within 10 s, requires minimal feedstock pretreatment, tolerates a wide range of SLCO degradation states, eliminates the need for external reductants, and enables near-complete recovery of lithium and cobalt. To address the intrinsic air sensitivity and oxygen evolution of L6CO, a uniform sulfur coating was introduced, which considerably enhances environmental stability and scavenging reactive oxygen species. The resulting L6CO@S composite exhibits enhanced processability, robust lithium-donating capability, and strong compatibility with both Gr||LFP and Gr||LCO systems, effectively boosting energy density, extending cycle life, and maintaining high Coulombic efficiency over prolonged operation.

Beyond its electrochemical merits, this upcycling approach offers compelling environmental and economic benefits. Compared to pyrometallurgical, hydrometallurgical, and direct recycling routes, it delivers the highest profit margin, lowest greenhouse gas emissions, and highest energy efficiency. Life-cycle analysis and successful scale-up to 1 Ah pouch cells confirm its practical feasibility and industrial relevance. Together, these findings establish a closed-loop, high-value recycling paradigm that integrates material recovery with

performance enhancement, offering a scalable and sustainable framework for next-generation lithium-ion battery lifecycle management.

Methods

Materials and upcycling process

Spent LCO pouch cells were collected from decommissioned mobile phones and laptops, sourced from Apple, Lenovo, ATL, and other manufacturers, with varying degrees of degradation. Spent LiCoO₂ (SLCO) batteries were first discharged to 1.0 V (vs. Li⁺/Li) and then soaked in 1.0 M sodium chloride (NaCl, 99%, Sigma–Aldrich) aqueous solution for 24 h to ensure complete discharge. Disassembly was performed inside an argon-filled glovebox. Recovered electrode foils were rinsed with dimethyl carbonate (DMC, 99%, Sigma–Aldrich) to remove residual electrolyte and lithium salts, then dried under inert atmosphere prior to further processing. The recovered SLCO electrodes were directly employed as working electrodes in a two-electrode electrolysis cell, with a mixed-metal oxide (MMO) mesh as the counter electrode owing to its high oxidation resistance. An aqueous solution composed of 0.5 M sodium sulfate (Na₂SO₄, 99%, Sigma–Aldrich) with 0.01 M sodium hydroxide (NaOH, 99%, Sigma–Aldrich) was employed as electrolyte. The electrolysis was conducted with a controlled current density of 50 mA cm⁻², and the process was terminated once the active material was completely detached. The separated materials were subsequently washed with deionized water, dried at 80 °C for 8 h, and gently ground. The obtained black mass consists of a mixture of SLCO, conductive carbon, and polyvinylidene fluoride (PVDF). While conventional recycling methods necessitate additional steps to eliminate these impurities, our upcycling approach can utilize these impurities as reducing agents during sintering. Hence, they do not require pre-removal. All chemical reagents were used as received.

To convert SLCO to Li₆CoO₄, 0.291 g of SLCO powder was mixed with 0.232 g of lithium oxide (Li₂O, 99.9%, Aladdin) and ground in an agate mortar for 15 min. The powder mixture was then pressed into 14 mm diameter pellets at 6 MPa and held for 5 min, sandwiched between carbon paper, and processed in a Joule heating device (Ultrafast High-Temperature Furnace 2022 A, Particle Precision instruments Co. Ltd, Jilin Province, China). The temperature was raised to 1200 °C within milliseconds and held for 10 s to yield Li₆CoO₄. For sulfur coating, the as-prepared Li₆CoO₄ powder was mixed with elemental sulfur (S, 99.95%, Aladdin) at a mass ratio of Li₆CoO₄:S = 10:1, hand milled for 15 min, sealed in a hydrothermal reactor under Ar, and heated in a vacuum oven at 160 °C for 6 h to produce L6CO@S.

Battery assembly and electrochemical tests

The LFP and LCO positive electrode slurry was prepared by mixing 80 wt.% active material (LFP from Hubei Wanrun and LCO from Shanshan Corporation), 10 wt.% conductive carbon (Super P, 99.9%, TIMCAL), and 10 wt.% PVDF (99.9%, Aladdin) in N-methyl-2-pyrrolidone (NMP, 99.9%, Aladdin). The slurry was stirred for 20 min in a homogenizer and then coated onto aluminum foil current collectors (15 μm thick, 99.9% purity). For batteries with additional lithium replenishment, L6CO or L6CO@S is directly added to the positive electrode slurry with an additional 4% mass fraction. After drying for 10 h under vacuum at 60 °C, the electrode was cut into 12 mm diameter discs for coin cell assembly. The graphite electrode was prepared similarly, with graphite (Dodochem), Super P, and PVDF mixed at a mass ratio of 9:0.5:0.5, and the slurry was coated onto copper foil (12 μm thick, 99.9% purity). The active materials mass loading of LFP electrodes was ~7 mg cm⁻², and the active materials mass loading of Gr electrodes was 3.65–4 mg cm⁻². The N/P ratio was set to 1.1 for the blank batteries and 1.2 for the batteries with lithium supply, respectively. The N/P ratio was calculated on the basis of the reversible capacities of the electrodes.

The CR2025 coin cells were assembled inside an Ar-filled glovebox (25 °C, O₂ and H₂O levels <1 ppm). Each cell was filled with 60 μL of

electrolyte (1M LiPF₆ dissolved in an ethylene carbonate (EC) and dimethyl carbonate (DMC) mixture (3:7 by volume) with 2 wt.% vinylene carbonate (VC)). Celgard A273 polypropylene membranes (16 μm thickness, 16.5 mm diameter, ~40% porosity, average pore size ~0.039 μm, from Celgard, LLC, USA) were used as separators and were dried at 60 °C for 12 h prior to cell assembly. The positive and negative cases, spring, and spacer, were purchased from Canrd Technology Co. Ltd. Assembly parameters for the 1Ah pouch cells are summarized in Supplementary Table 5. All coin cells and pouch cells were rested for 8 h to ensure sufficient electrolyte permeation before electrochemical tests. The electrochemical characterizations were carried out at 25 °C using a NEWARE Battery Testing System (MIHW-200-160, Shenzhen, China). Electrochemical impedance spectroscopy (EIS) and cyclic voltammetry (CV) experiments were performed using a GAMRY INTERFACE 1010E electrochemical workstation. EIS measurements were conducted under potentiostatic conditions at open-circuit voltage after the resting period, using an AC amplitude of 10 mV over a 100 kHz–0.1 Hz frequency window with 10 points per decade. The CV scan rate was 0.05 mV s⁻¹. The GITT measurements were conducted with the titration step at 0.1C for 20 min and a relaxation step of 1 h.

Materials characterization

The composition of SLCO and upcycled materials was determined using inductively coupled plasma optical emission spectroscopy (ICP-OES) (Agilent 5800), while phase compositions were analyzed via X-ray diffraction (XRD) (Bruker D8 Advance) using Cu Kα radiation in the 2θ range of 10–80°. The Fourier transform infrared spectroscopy (FTIR) patterns were tested using the Bruker INVENIO FT-IR analysis platform. Scanning electron microscopy (SEM) (FEI, QUANTA 250FEG), transmission electron microscopy (TEM) (Tecnai F30), and cryo-TEM (Thermo Fisher Scientific Titan Krios, operated at 300 kV and equipped with a K3 Summit direct electron detection camera, Gatan) were employed to observe the morphology and microstructure of the samples. Energy-dispersive spectroscopy (EDS) mapping was used to analyze the distribution of elements in the particles. The valence state change of sulfur during charging was monitored using X-ray photoelectron spectroscopy (XPS) (Thermo Fisher Scientific Escalab 250Xi) and X-ray absorption spectroscopy (XAS) techniques. XAS data were collected at Shanghai Synchrotron Radiation Facility (SSRF, China). The cells for XAS measurements were disassembled in an argon-filled glovebox, and the electrodes were sealed with Kapton tape and Mylar film to prevent exposure to air. Online differential electrochemical mass spectrometry (OEMS) (QAS 100, Shanghai Linglu Instruments Co., Ltd.) was employed to observe gas evolution during the charging process. Capillary electrophoresis (CE) (P/ACE MDQ capillary electrophoresis system equipped with a UV detector) analysis was conducted to quantitatively determine SO₄²⁻. The charged electrodes were soaked in deionized water, and the resulting suspension was filtered to obtain the supernatant for analysis. An ultrasonic battery scanner (Wuxi Topsound Technology Co., Ltd.) was used to detect gas generation and distribution within pouch cells.

Theoretical calculations

First-principle calculations were conducted within a plane-wave density-functional theory (DFT) framework. The exchange-correlation potential was treated using the Perdew, Burke, and Ernzerhof (PBE) method of the generalized gradient approximation (GGA). A cutoff energy of 450 eV was adopted for the plane-wave, and the electronic and ionic relaxations were converged to 10⁻⁵ eV in solving the Kohn-Sham equations. For all models, a vacuum space of 15 Å was applied along the z-direction to avoid interactions between neighboring images. Sampling of the Brillouin zone was performed using a 2 × 2 × 1 k-point grid. All atomic structures were relaxed until the maximum residual force on each atom was below 0.02 eV/Å. Dispersion-corrected DFT calculations were also employed to account for van

der Waals interactions. The adsorption strength between the surface and adsorbates was quantified based on the adsorption energy, defined as:

$$\Delta E_{\text{ads}} = \Delta E_{(\text{adsorb}/\text{surf})} - \Delta E_{(\text{surf})} - \Delta E_{(\text{adsorb})}$$

Where $\Delta E_{(\text{adsorb}/\text{surf})}$, $\Delta E_{(\text{surf})}$ and $\Delta E_{(\text{adsorb})}$ correspond to the calculated total energies of the substrate with adsorbate(s), the clean substrate, and the isolated adsorbate, respectively.

All optimized atomic configurations used in the above calculations are provided in Supplementary Data 1.

Economic analysis of different battery recycling technologies

EverBatt developed by Argonne National Laboratory was used to evaluate the cost, profit, energy consumption, and GHG emissions of pyro-, hydro-, direct recycling, and our upcycling method. A total of 10,000 tonnes of end-of-life LCO batteries were input for preprocessing, with the separated black mass processed via various recycling methods. A detailed assessment of raw material costs and potential product revenues is provided in Supplementary Tables 6–11. Due to the high lithium content in L6CO, the raw material costs, particularly for lithium salts, are higher than in other recycling methods. The market price for L6CO was estimated based on the price of LFO. Additionally, the GHG emissions and total energy consumption of the different processes were evaluated, as detailed in Supplementary Table 12.

Data availability

Source data are provided with this paper.

References

- Liu, Q. et al. Approaching the capacity limit of lithium cobalt oxide in lithium ion batteries via lanthanum and aluminium doping. *Nat. Energy* **3**, 936–943 (2018).
- Li-ion Battery Recycling Market 2025-2045: Markets, Forecasts, Technologies, and Players, <<https://www.idtechex.com/en/research-report/li-ion-battery-recycling-market/1090>> (2025).
- Wang, J. et al. Toward direct regeneration of spent lithium-ion batteries: A Next-Generation Recycling Method. *Chem. Rev.* **124**, 2839–2887 (2024).
- Ciez, R. E. & Whitacre, J. F. Examining different recycling processes for lithium-ion batteries. *Nat. Sustain.* **2**, 148–156 (2019).
- Chen, M. et al. Recycling end-of-life electric vehicle lithium-ion batteries. *Joule* **3**, 2622–2646 (2019).
- Tran, M. K., Rodrigues, M.-T. F., Kato, K., Babu, G. & Ajayan, P. M. Deep eutectic solvents for cathode recycling of Li-ion batteries. *Nat. Energy* **4**, 339–345 (2019).
- Ma, X. et al. The evolution of lithium-ion battery recycling. *Nat. Rev. Clean. Technol.* **1**, 75–94 (2025).
- Ogihara, N. et al. Direct capacity regeneration for spent Li-ion batteries. *Joule* **8**, 1364–1379 (2024).
- Wang, J. et al. Direct recycling of spent cathode material at ambient conditions via spontaneous lithiation. *Nat. Sustain.* **7**, 1283–1293 (2024).
- Harper, G. et al. Recycling lithium-ion batteries from electric vehicles. *Nature* **575**, 75–86 (2019).
- Tang, J. et al. A universal solution for direct regeneration of spent lithium iron phosphate. *Adv. Mater.* **37**, 2420238 (2025).
- Ji, G. et al. Direct regeneration of degraded lithium-ion battery cathodes with a multifunctional organic lithium salt. *Nat. Commun.* **14**, 584 (2023).
- Zheng, M., You, Y. & Lu, J. Understanding materials failure mechanisms for the optimization of lithium-ion battery recycling. *Nat. Rev. Mater.* **10**, 355–368 (2025).

14. Wang, J. et al. Sustainable upcycling of spent LiCoO₂ to an ultra-stable battery cathode at high voltage. *Nat. Sustain.* **6**, 797–805 (2023).
 15. Chen, W. et al. Nondestructive flash cathode recycling. *Nat. Commun.* **15**, 6250 (2024).
 16. Qiao, Y. et al. A high-energy-density and long-life initial-anode-free lithium battery enabled by a Li₂O sacrificial agent. *Nat. Energy* **6**, 653–662 (2021).
 17. Sun, Y. et al. High-capacity battery cathode prelithiation to offset initial lithium loss. *Nat. Energy* **1**, 15008 (2016).
 18. Chen, S. et al. External Li supply reshapes Li deficiency and lifetime limit of batteries. *Nature* **638**, 676–683 (2025).
 19. Jun, K. et al. Understanding the Irreversible Reaction Pathway of the Sacrificial Cathode Additive Li₆CoO₄. *Adv. Energy Mater.* **13**, 2301132 (2023).
 20. Park, H., Yoon, T., Kim, Y.-U., Ryu, J. H. & Oh, S. M. Li₂NiO₂ as a sacrificing positive additive for lithium-ion batteries. *Electrochim. Acta* **108**, 591–595 (2013).
 21. Zhan, C. et al. Enabling the high capacity of lithium-rich anti-fluorite lithium iron oxide by simultaneous anionic and cationic redox. *Nat. Energy* **2**, 963–971 (2017).
 22. Zhu, B. et al. Understanding the Air-Exposure Degradation Chemistry of the Sacrificial Cathode Additive Li₅FeO₄ for Li-Ion Batteries. *Adv. Funct. Mater.* **34**, 2315010 (2024).
 23. Liu, C. et al. Air-stable Li₅FeO₄ additive enabled by carbon coating for energy-dense lithium-ion batteries. *Nat. Commun.* **16**, 7694 (2025).
 24. Liu, T. et al. Origin of structural degradation in Li-rich layered oxide cathode. *Nature* **606**, 305–312 (2022).
 25. Gao, X. et al. Clarifying the origin of molecular O₂ in cathode oxides. *Nat. Mater.* **24**, 743–752 (2025).
 26. Zhu, Y. et al. Unravelling the oxygen evolution mechanism of lithium-rich antiferroite prelithiation agent based on anionic oxidation. *Angew. Chem. Int. Ed.* **137**, e202502126 (2025).
 27. Mahne, N. et al. Singlet oxygen generation as a major cause for parasitic reactions during cycling of aprotic lithium–oxygen batteries. *Nat. Energy* **2**, 17036 (2017).
 28. Zhang, K. et al. Sulfuration of Li-rich mn-based cathode materials for multianionic redox and stabilized coordination environment. *Adv. Mater.* **34**, 2109564 (2022).
 29. Tian, M. et al. Designer lithium reservoirs for ultra-long life lithium batteries for grid storage. *Adv. Mater.* **36**, 2400707 (2024).
 30. Yang, F. et al. Electrode separation via water electrolysis for sustainable battery recycling. *Nat. Sustain.* **8**, 520–529 (2025).
 31. Mao, J. et al. Toward practical lithium-ion battery recycling: adding value, tackling circularity and recycling-oriented design. *Energy Environ. Sci.* **15**, 2732–2752 (2022).
 32. Cai, M. et al. Stalling oxygen evolution in high-voltage cathodes by lanthanization. *Nat. Energy* **8**, 159–168 (2023).
 33. Wang, Q. et al. Direct observation of sulfur radicals as reaction media in lithium sulfur batteries. *J. Electrochem. Soc.* **162**, A474–A478 (2015).
- C.W.), Natural Science Foundation of Shanghai (grant no. 25ZR1401358 to C.W.), and the Fundamental Research Funds for the Central Universities. We also thank the Shanghai Synchrotron Radiation Facility (BL16U1, <https://cstr.cn/31124.02.SSRF.BL16U1>) for the assistance on XAS measurements.

Author contributions

G.L. and Q.N. contributed equally to this work. G.L., C.W., and Y.H. conceived the research idea. G.L., Q.N., and W.W. designed and performed the experiments. G.L. and F.Y. carried out material synthesis and electrochemical testing. Q.N., W.W., L.G., Z.Y., G.Q., and J.C. assisted with material characterization and data processing. X.W., C.W., and Y.H. contributed to manuscript revision. All authors discussed the results and contributed to data analysis. G.L. and Q.N. wrote the manuscript with input from all authors. J.C., X.W., C.W., and Y.H. supervised the project.

Competing interests

The authors declare no competing interests.

Additional information

Supplementary information The online version contains supplementary material available at <https://doi.org/10.1038/s41467-025-67496-9>.

Correspondence and requests for materials should be addressed to Jitao Chen, Xuezhe Wei, Yunhui Huang or Chao Wang.

Peer review information *Nature Communications* thanks Junxiang Wang, Weiyin Chen and the other, anonymous, reviewer(s) for their contribution to the peer review of this work. A peer review file is available.

Reprints and permissions information is available at <http://www.nature.com/reprints>

Publisher's note Springer Nature remains neutral with regard to jurisdictional claims in published maps and institutional affiliations.

Open Access This article is licensed under a Creative Commons Attribution-NonCommercial-NoDerivatives 4.0 International License, which permits any non-commercial use, sharing, distribution and reproduction in any medium or format, as long as you give appropriate credit to the original author(s) and the source, provide a link to the Creative Commons licence, and indicate if you modified the licensed material. You do not have permission under this licence to share adapted material derived from this article or parts of it. The images or other third party material in this article are included in the article's Creative Commons licence, unless indicated otherwise in a credit line to the material. If material is not included in the article's Creative Commons licence and your intended use is not permitted by statutory regulation or exceeds the permitted use, you will need to obtain permission directly from the copyright holder. To view a copy of this licence, visit <http://creativecommons.org/licenses/by-nc-nd/4.0/>.

© The Author(s) 2026

Acknowledgements

We acknowledge support from the National Key Research and Development Program of China (grant no. 2022YFB3803400 to C.W.), National Natural Science Foundation of China (grant no. 22579129 to